Vorticity structuring and velocity rolls triggered by gradient shear bands

Suzanne M. Fielding*

School of Mathematics and Manchester Centre for Nonlinear Dynamics, University of Manchester, Booth Street East, Manchester M13 9EP, United Kingdom

(Received 26 June 2006; revised manuscript received 6 March 2007; published 23 July 2007; publisher error corrected 26 July 2007)

We suggest a mechanism by which vorticity structuring and velocity rolls can form in complex fluids, triggered by the linear instability of one-dimensional gradient shear banded flow. We support this with a numerical study of the diffusive Johnson-Segalman model. In the steady vorticity structured state, the thickness of the interface between the bands remains finite in the limit of zero stress diffusivity, presenting a possible challenge to the accepted theory of shear banding.

DOI: 10.1103/PhysRevE.76.016311 PACS number(s): 47.50.−d, 36.20.−r, 47.20.−k

I. INTRODUCTION

Many complex fluids exhibit flow instabilities that result in spatially heterogeneous, shear banded states. Examples include wormlike [1–3] and onion [4–6] surfactants; side-chain liquid crystalline polymers [7]; viral suspensions [8,9]; telechelic polymers [10]; soft glasses [11]; polymer solutions [12]; and colloidal suspensions [13]. In many cases, the instability is explained by a region of negative slope $dT_{xy}/d\dot{\gamma} < 0$ in the constitutive relation $T_{xy}(\dot{\gamma})$ between shear stress and shear rate for homogeneous flow, as shown in Fig 1(a). In this regime, homogeneous flow is unstable [14] with respect to the formation of bands of differing shear rates $\dot{\gamma}_1$ and $\dot{\gamma}_2$, with layer normals in the flow-gradient direction. Force balance requires that the shear stress T_{xy} is uniform across the gap, and therefore common to both bands. Any change in the overall applied shear rate $\bar{\dot{\gamma}}$ causes a change in the relative volume fraction f of the bands according to a lever rule $\bar{\dot{\gamma}} = f\dot{\gamma}_1 + (1-f)\dot{\gamma}_2$, while $\dot{\gamma}_1, \dot{\gamma}_2$, and T_{xy} remain constant. In bulk rheometry, this leads to a plateau in the steady state flow curve at some stress $T_{xy} = T^*$ [Fig. 1(a)], the value of which is selected by accounting for spatial nonlocality in the constitutive dynamics of the viscoelastic stress [15]. In what follows, we shall refer to the effect just described as gradient shear banding or simply gradient banding.

In some systems, flow induced heterogeneity has instead been reported in the vorticity direction. By analogy with the above discussion, this effect is often termed vorticity banding. It has been observed in onion surfactants [4,16] and colloidal crystals [13], accompanied by a steep stress "cliff" in the flow curve. Multiple turbid and clear vorticity bands also occur in some polymeric [12] and micellar [17,18] solutions, accompanied by shear thickening. In these cases, the bands not only alternate in space but also oscillate in time. In shear thinning viral suspensions, multiple stationary vorticity bands can arise in the regime of isotropic-nematic phase coexistence [8,9].

In comparison with gradient banding, vorticity banding is poorly understood theoretically. To date, the main attempts to model it have invoked the analogy with gradient banding [19]. As discussed above, gradient bands have different shear rates $\dot{\gamma}_1, \dot{\gamma}_2$, and coexist at a common shear stress T^*. For vorticity bands, the moving rotor imposes a shear rate that is common to each band. Pursuing the analogy with gradient banding, it is natural to invoke an underlying constitutive curve of the form in Fig. 1(b), in the case of shear thickening systems. This allows bands (A and B) of differing shear stresses to coexist, having layer normals in the vorticity direction. In steady state, one then expects a flow curve with a steep stress cliff, consistent with the experimental observations discussed above [4,13,16]. This scenario can be adapted to shear thinning systems by invoking a constitutive curve of the form sketched in Fig. 1(c). In fact, at the level of one-dimensional (1D) calculations performed separately in the flow-gradient and vorticity directions, such a curve can support either gradient or vorticity banded states [20]. Which of these (if either) would be selected in a full 3D calculation remains an outstanding question. Indeed, any concrete calculation of vorticity banding to date has taken a simplified 1D approach, allowing spatial variations only in the direction of the layer normals, and thereby imposing axial and radial symmetry.

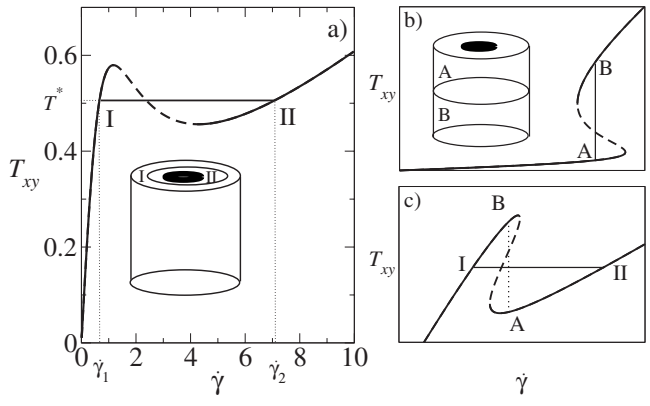

FIG. 1. (a) Homogeneous constitutive curve and steady state flow curve for 1D planar gradient banded flow in the DJS model at $a=0.3, \eta=0.05$. Inset: schematic arrangement of the bands in curved Couette flow. (b) Schematic constitutive curve giving shear thickening vorticity banding. (c) A shear thinning curve allowing gradient or vorticity banding in 1D.

*suzanne.fielding@manchester.ac.uk

Beyond the traditional shear banding literature, other flow instabilities are well known to trigger structuring in the vorticity direction, in both simple and complex fluids. For simple liquids in curved Couette flow, the unstable centripetal interplay of fluid inertia with cell curvature gives rise to Taylor velocity rolls [21] stacked in the vorticity direction. An analogous inertia-free instability occurs in viscoelastic fluids, here triggered by viscoelastic hoop stresses [22,23], and again leading to velocity rolls stacked along the axis of the Couette cylinder. The rolls are typically observed as bandlike structures, imaged by seeding the fluid with mica flakes.

In contrast to the 1D vorticity banding scenario discussed above, both traditional and viscoelastic Taylor-Couette instabilities are inherently 2D (at least), with velocity rolls comprising a circulation of fluid in the flow-gradient–vorticity plane [21,22]. Not unexpectedly, given this roll-like structure, the wavelength of the associated banding in the vorticity direction is roughly set by the width of the gap in the flow-gradient direction [21].

In view of the above discussion, it is natural to ask whether any link exists between traditional (1D) vorticity banding and 2D viscoelastic Taylor-Couette instabilities; or whether the two effects are entirely distinct. Given that both can be accompanied by shear thickening in the bulk flow curve, this is a difficult question to address experimentally. Even if they are distinct in theory, it seems feasible that some experimental observations that have traditionally been interpreted as 1D vorticity banding in fact comprise 2D viscoelastic Taylor Couette rolls. Likely candidates include those systems in which the wavelength of the alternating vorticity bands is comparable to the width of the cell in the flow-gradient direction, suggesting an underlying roll structure [8,9,12,17,18]. This was recently suggested in the context of viral suspensions in Ref. [24]. In other systems, particularly those showing a very marked stress cliff in flow curve, the traditional 1D scenario of Fig. 1(b) and 1(c) remains more likely.

In this paper, we suggest a novel mechanism by which vorticity structuring can emerge in complex fluids. A key feature of our approach is that, to some extent, it unifies traditional 1D (gradient) banding descriptions with those of 2D roll-like instabilities. The basic idea is as follows. The constitutive curve of Fig. 1(a) gives rise initially to 1D gradient bands, via the conventional instability in the region of negative slope $dT_{xy}/d\dot{\gamma}<0$. These then undergo a secondary linear instability [25,26], due to the action of normal stresses across the interface between the bands. This leads finally to pronounced undulations along the interface, with wave vector in the vorticity direction. These are accompanied by 2D velocity rolls stacked in the vorticity direction, and undulatory vorticity stress structuring superposed on the underlying gradient bands. In contrast to the conventional inertial [21] and viscoelastic [22] Taylor mechanisms, the vorticity instability introduced here does not rely on cell curvature, but occurs even in the limit of planar shear, to which our calculations are confined for simplicity.

The results to be presented are in good agreement with recent experiments in which a gradient banded solution of wormlike micelles was found to be unstable with respect to interfacial undulations with the wave vector in the vorticity direction [27]. We will return to a detailed comparison with these experiments later. Our results might also apply to systems in which shear thickening [28] and/or vorticity banding [12,16–18] is reported to set in at the right hand edge of a stress plateau in the flow curve [suggestive of underlying gradient banding, as in Fig. 1(a)] or in which gradient and vorticity banding have actually been observed concomitantly [29].

The paper is structured as follows. In Sec. II we introduce the diffusive Johnson Segalman (DJS) model, within which the subsequent calculations are to be performed. In Sec. III we discuss 1D calculations, confined to the flow-gradient direction. These predict gradient banding for applied shear rates in the regime of negative slope in the homogeneous constitutive curve. In Sec. IV we switch to two dimensions—the flow-gradient–vorticity plane—and show an initially 1D gradient banded "base state" to be linearly unstable with respect to undulations along the interface with wavevector in the vorticity direction. We then perform a full 2D nonlinear numerical study of the subsequent growth and eventual saturation of these undulations. Details of the numerical method are discussed in Sec. V, followed by presentation of the results in Sec. VI. Finally we summarize our findings and discuss some directions for future study.

II. MODEL AND GEOMETRY

The generalized Navier-Stokes equation for a viscoelastic material in a Newtonian solvent of viscosity η and density ρ is

$$\rho(\partial_t + \mathbf{v}\cdot\boldsymbol{\nabla})\mathbf{v} = \boldsymbol{\nabla}\cdot(\boldsymbol{\Sigma} + 2\eta\mathbf{D} - P\mathbf{I}), \tag{1}$$

where $\mathbf{v}(\mathbf{r},t)$ is the velocity field and $\mathbf{D}$ is the symmetric part of the velocity gradient tensor, $(\boldsymbol{\nabla}\cdot\mathbf{v})_{\alpha\beta}\equiv\partial_\alpha v_\beta$. The pressure field $P(\mathbf{r},t)$ is determined by enforcing incompressibility

$$\boldsymbol{\nabla}\cdot\mathbf{v} = 0. \tag{2}$$

The quantity $\boldsymbol{\Sigma}(\mathbf{r},t)$ in Eq. (1) is the extra stress contributed by the viscoelastic component. In principle, the dynamics of this quantity should be explicitly derived by averaging over the underlying microscopic dynamics of the viscoelastic component. This was done in Ref. [30] for wormlike micelles. For simplicity, however, we use the phenomenological Johnson-Segalman (JS) model [31]

$$(\partial_t + \mathbf{v}\cdot\boldsymbol{\nabla})\boldsymbol{\Sigma} = a(\mathbf{D}\cdot\boldsymbol{\Sigma} + \boldsymbol{\Sigma}\cdot\mathbf{D}) + (\boldsymbol{\Sigma}\cdot\boldsymbol{\Omega} + \boldsymbol{\Omega}\cdot\boldsymbol{\Sigma}) + 2G\mathbf{D} - \frac{\boldsymbol{\Sigma}}{\tau} + \frac{l^2}{\tau}\boldsymbol{\nabla}^2\boldsymbol{\Sigma}. \tag{3}$$

In this equation, G is a plateau modulus, τ is the viscoelastic relaxation time, and $\boldsymbol{\Omega}$ is the antisymmetric part of the velocity gradient tensor. For $a=1$ and $l=0$, Eq. (3) reduces to the Oldroyd B model, which can be derived by considering the dynamics of an ensemble of Hookean dumb-bells in solution. For $|a|<1$, the JS model captures nonaffine slip between the dumbbells and the solvent, leading to the drastic shear thinning of Fig. 1(a). Accordingly, a is called the slip

parameter. The JS model is the simplest tensorial model to exhibit a regime of negative slope in the homogeneous constitutive curve, and so to predict a shear banding instability. As discussed further below, the diffusive term $\nabla^2\boldsymbol{\Sigma}$ in Eq. (3) is needed to correctly describe the ultimate shear banded flow [15].

Within this model, we study planar shear between parallel plates at $y=0,L$, with the top plate driven at velocity $V\hat{\mathbf{x}}$. At the plates we assume boundary conditions of $\partial_y\Sigma_{\alpha\beta}=0\,\forall\,\alpha,\beta$ for the viscoelastic stress, with no slip and no permeation for the fluid velocity. In the linear stability analysis of Sec. IV, we consider small values of the Reynolds number $\mathrm{Re}=\rho L^2/\eta$. In the nonlinear study of Secs. V and VI, we set $\mathrm{Re}=0$ at the outset. Throughout we use units in which $G=1$, $\tau=1$, and $L=1$.

III. 1D GRADIENT BANDS

As noted above, to capture shear thinning the DJS model invokes a slip parameter a with $|a|<1$, giving nonaffine deformation of the viscoelastic component [31]. The homogeneous constitutive curve $T_{xy}=\Sigma_{xy}(\dot{\gamma},a)+\eta\dot{\gamma}$ is then capable of nonmonotonicity, as in Fig. 1(a). For an imposed shear rate $\bar{\dot{\gamma}}\equiv V/L$ in the region of decreasing stress, homogeneous flow is unstable with respect to fluctuations with wavevector in the flow-gradient direction y [32]. A 1D calculation then predicts separation into gradient bands of differing shear rates $\dot{\gamma}_1,\dot{\gamma}_2$, with a flat interface in between. The diffusive term in Eq. (3) is needed to account for spatial gradients of the shear rate and viscoelastic stress across the interface, which has a characteristic thickness $O(l)$. It also ensures a unique, history-independent banding stress $T_{xy}=T^*$ [15], as seen experimentally. We expect $l=O(10^{-4})$, set by the typical micellar mesh size, in units of the (typical) gap size.

IV. LINEAR INSTABILITY

In Refs. [25,26], we considered the linear stability of this 1D gradient banded state with respect to 3D (x,y,z) perturbations of infinitesimal amplitude. In the flow direction $\hat{\mathbf{x}}$ and vorticity direction $\hat{\mathbf{z}}$ these are decomposed into Fourier modes with wave vectors $\mathbf{q}=q_x\hat{\mathbf{x}}+q_z\hat{\mathbf{z}}$. Reference [33] had previously considered $\mathbf{q}=q_x\hat{\mathbf{x}}$ in the pathological limit $\ell=0$, assuming "top jumping". For diffuse interfaces, $l\gtrsim 0.015$, the 1D state is linearly stable. For $l\lesssim 0.015$, we find it to be linearly unstable with respect to modes with wave vector $\mathbf{q}=q_x\hat{\mathbf{x}}$ in the flow direction [25,26]. The associated eigenfunction essentially corresponds to undulations along the interface. For $l\lesssim 0.005$, the 1D state is also unstable with respect to undulations with wave vector $\mathbf{q}=q_z\hat{\mathbf{z}}$ in the vorticity direction. However, these modes are predicted to grow much more slowly than those with $\mathbf{q}=q_x\hat{\mathbf{x}}$. Accordingly, in Refs. [25,26], we focused mainly on the dominant modes, $\mathbf{q}=q_x\hat{\mathbf{x}}$. Subsequently in Ref. [34], however, we showed that these undulations are cut off, once they attain finite amplitude, by the nonlinear effects of shear. In contrast, the vorticity direction is neutral with respect to the shear. Accordingly, the modes with $\mathbf{q}=q_z\hat{\mathbf{z}}$ should not suffer this cutoff and are therefore likely to contribute significantly to the ultimate nonlinear state, despite their much slower initial growth rate. With this motivation, in this paper we study the dynamics of the model in the flow-gradient–vorticity $(y-z)$ plane. For simplicity and computational efficiency, we will assume uniformity in the flow direction x, returning in Sec. VI below to comment on the validity of this simplification. It corresponds to taking a vertical slice through one side of an axisymmetric flow state in the planar limit of a Couette device.

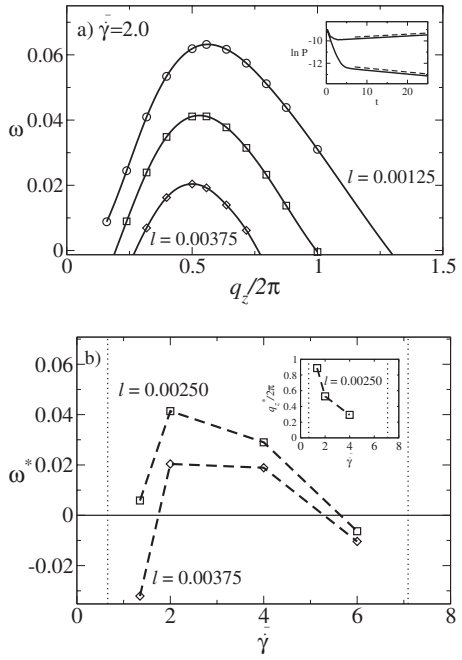

FIG. 2. (a) Dispersion relation for perturbations about a 1D banded state for $l=0.00375$, 0.00250, 0.00125. $a=0.3$, $\eta=0.05$, $\rho/\eta=0.02$. Inset: Linear dynamics of 2D code, starting from a flat interface. Solid lines: weight in modes, $q_zL_z/2\pi=1,2$; dashed: analytical prediction. (b) Peak ω^* (q^* in inset) in dispersion relation vs $\bar{\dot{\gamma}}$ across the plateau of Fig. 1(a). Vertical dashed lines denote the edges of the stress plateau.

The growth rates ω of the vorticity modes $\mathbf{q}=q_z\hat{\mathbf{z}}$ are shown in Fig. 2(a), at a single value of the imposed shear rate. States with thinner interfaces (smaller l) are more unstable (larger $\omega>0$). Figure 2(b) shows the growth rate of the maximally unstable mode for shear rates across the stress plateau of Fig. 1(a). The corresponding wavelength $\lambda^*=O(1)$ is of order the rheometer gap $L\equiv 1$ (inset). At small l, the instability persists across most of the plateau, so is likely to be unavoidable experimentally. The mechanism of instability is not fully understood, but is likely to stem from steep gradients in the normal stress and shear rate across the interface [25,35,36].

V. NUMERICAL METHOD

To study the undulations once they have grown to attain a finite amplitude, beyond the regime of linear instability, we solve the model's full nonlinear dynamics numerically. In this section we discuss the details of our numerical method, which is adapted from that of Refs. [34,37]. Readers who are

not interested in these issues can skip straight to Sec. VI without loss of thread.

The model equations have already been specified in Sec. II, together with the flow geometry, boundary conditions and choice of adimensionalization. For computational efficiency, our numerical study is confined to the $(y\text{-}z)$ plane, assuming translational invariance along the flow direction x. In the vorticity direction we take a cell of length L_z, with periodic boundary conditions.

We consider the limit of zero Reynolds number, in which Eq. (1) reduces to

$$0 = \nabla \cdot (\boldsymbol{\Sigma} + 2\eta \mathbf{D} - P\mathbf{I}). \tag{4}$$

To ensure that the incompressibility constraint of Eq. (2) is satisfied always, we express the velocity in terms of stream functions ϕ and ψ:

$$v_x = \partial_y \phi, \quad v_y = \partial_z \psi, \quad v_z = -\partial_y \psi. \tag{5}$$

In this way, Eq. (2) need no longer be considered, leaving only Eqs. (3) and (4), with the velocity expressed as in Eq. (5).

To solve these, the basic strategy is to step along a grid of time values $t^n = n\Delta t$ for $n = 1, 2, 3, \ldots$, at each step updating $\boldsymbol{\Sigma}^n$, ϕ^n, $\psi^n \rightarrow \boldsymbol{\Sigma}^{n+1}$, ϕ^{n+1}, ψ^{n+1}. Discretization with respect to time of any quantity f is denoted $f(t^n) = f^n$, or sometimes by $f|^n$. At each time-step, we first update the viscoelastic stress $\boldsymbol{\Sigma}^n \rightarrow \boldsymbol{\Sigma}^{n+1}$ using the constitutive equation (3) with fixed, old values of the stream functions ϕ^n, ψ^n. We then update ϕ^n, $\psi^n \rightarrow \phi^{n+1}, \psi^{n+1}$ using the force balance equation (4) with the new values of $\boldsymbol{\Sigma}^{n+1}$.

The update $\boldsymbol{\Sigma}^n \rightarrow \boldsymbol{\Sigma}^{n+1}$ using the viscoelastic constitutive equation (3) is performed as follows. As a preliminary step, we rewrite Eq. (3) in the form

$$\partial_t \boldsymbol{\Sigma} = f(\nabla \cdot \mathbf{v}, \boldsymbol{\Sigma}) - \mathbf{v} \cdot \nabla \boldsymbol{\Sigma} + l^2 \nabla^2 \boldsymbol{\Sigma}, \tag{6}$$

in which $f(\nabla \cdot \mathbf{v}, \boldsymbol{\Sigma})$ comprises the nondiffusive terms from the right-hand side of Eq. (3). In what follows, the three terms on the right hand side of Eq. (6) are referred to as the local, advective, and diffusive terms, respectively. Numerically, they are dealt with in three successive partial updates $\boldsymbol{\Sigma}^n \rightarrow \boldsymbol{\Sigma}^{n+1/3}$, $\boldsymbol{\Sigma}^{n+1/3} \rightarrow \boldsymbol{\Sigma}^{n+2/3}$, and $\boldsymbol{\Sigma}^{n+2/3} \rightarrow \boldsymbol{\Sigma}^{n+1}$.

In the first of these, the local term is handled using an explicit Euler algorithm [38], checked for consistency against a fourth order Runge-Kutta algorithm [38]. Temporarily setting aside the issue of spatial discretization, the Euler algorithm can be written

$$\boldsymbol{\Sigma}^{n+1/3}(y,z) = \boldsymbol{\Sigma}^n + \Delta t f(\nabla \cdot \mathbf{v}^n, \boldsymbol{\Sigma}^n). \tag{7}$$

In terms of the stream functions ϕ and ψ, the velocity-gradient tensor $\nabla \cdot \mathbf{v}$ has Cartesian components

$$\nabla \cdot \mathbf{v} = \begin{pmatrix} 0 & 0 & 0 \\ \partial_y^2 \phi & \partial_y \partial_z \psi & -\partial_y^2 \psi \\ \partial_y \partial_z \phi & \partial_z^2 \psi & -\partial_y \partial_z \psi \end{pmatrix}, \tag{8}$$

in which we have omitted the superscripts n for clarity. Equations (7) and (8) are then spatially discretized on a rectangular grid in real space. In some runs of the code, the grid points are linearly spaced, with $z_i = i\Delta z$ for $i = 1, \ldots, N_z$, and $y_j = j\Delta y$ for $j = 1, \ldots, N_y$. In others, we used a nonlinear mapping in the y direction to focus attention on the region explored by the interface. For simplicity, most of the description of this section will concern the linear grid, though we will return briefly at the end of the section to discuss the nonlinear modification. In either case, any spatially discretized function f is denoted $f(y^j, z^i) = f_{ij}$, or sometimes $f|_{ij}$. (The apparently unusual order of the indices is a historical convention on the part of the author, stemming from a previous study in the x-y plane.) Equation (7) then becomes

$$\boldsymbol{\Sigma}_{ij}^{n+1/3} = \boldsymbol{\Sigma}_{ij}^n + \Delta t f(\nabla \cdot \mathbf{v}_{ij}^n, \boldsymbol{\Sigma}_{ij}^n) \tag{9}$$

The derivatives in the components of $\nabla \cdot \mathbf{v}_{ij}^n$ are discretized (in the case of a rectangular grid) as follows:

$$\partial_y^2 \psi|_{ij}^n = \frac{1}{(\Delta y)^2}[\psi_{i(j+1)}^n - 2\psi_{ij}^n + \psi_{i(j-1)}^n], \tag{10}$$

$$\partial_z^2 \psi|_{ij}^n = \frac{1}{(\Delta z)^2}[\psi_{(i+1)j}^n - 2\psi_{ij}^n + \psi_{(i-1)j}{}^n], \tag{11}$$

and

$$\partial_y \partial_z \psi|_{ij}^n = \frac{1}{4\Delta y \Delta z}[\psi_{(i+1)(j+1)} - \psi_{(i+1)(j-1)} - \psi_{(i-1)(j+1)} + \psi_{(i-1)(j-1)}]. \tag{12}$$

Corresponding derivatives of ϕ are obtained in the same way, replacing ψ by ϕ in the above equations. For values of ij at the edges of the flow domain, these formulae link to values of the flow variables at "phantom" grid points that lie just outside the domain. These values are specified by imposing the boundary conditions, the spatial discretization of which is discussed at the end of this section.

The advective term is also handled using an explicit Euler algorithm [38], on the same real space grid:

$$\boldsymbol{\Sigma}_{ij}^{n+2/3} = \boldsymbol{\Sigma}_{ij}^{n+1/3} - \Delta t\left(v_y|_{ij}^n \partial_y \boldsymbol{\Sigma}|_{ij}^n + v_z|_{ij}^n \partial_z \boldsymbol{\Sigma}|_{ij}^n\right) = \boldsymbol{\Sigma}_{ij}^{n+1/3} - \Delta t\left(\partial_z \psi|_{ij}^n \partial_y \boldsymbol{\Sigma}|_{ij}^n - \partial_y \psi|_{ij}^n \partial_z \boldsymbol{\Sigma}|_{ij}^n\right). \tag{13}$$

The derivatives of ψ in this equation are discretized as follows:

$$\partial_y \psi|_{ij}^n = \frac{1}{2\Delta y}[\psi_{i(j+1)} - \psi_{i(j-1)}] \quad \text{and} \quad \partial_z \psi|_{ij}^n = \frac{1}{2\Delta z}[\psi_{(i+1)j} - \psi_{(i-1)j}]. \tag{14}$$

The derivative of $\boldsymbol{\Sigma}$ with respect to y in Eq. (13) was discretized using third-order upwinding [39]

$$\partial_y \boldsymbol{\Sigma}_{ij}^n = \frac{1}{6\Delta y}[\boldsymbol{\Sigma}_{i(j-2)}^n - 6\boldsymbol{\Sigma}_{i(j-1)}^n + 3\boldsymbol{\Sigma}_{ij}^n + 2\boldsymbol{\Sigma}_{i(j+1)}^n] \quad \text{if} \quad v_y|_{ij}^n > 0, \tag{15}$$

while

$$\partial_y \Sigma_{ij}^n = \frac{1}{6\Delta y}[-\Sigma_{i(j+2)}^n + 6\Sigma_{i(j+1)}^n - 3\Sigma_{ij}^n - 2\Sigma_{i(j-1)}^n] \quad \text{if} \quad v_y|_{ij}^n < 0, \tag{16}$$

with analogous expressions for the derivative of $\boldsymbol{\Sigma}$ with respect to z.

The diffusive term is handled by discretizing on y in real space as above, taking a fast Fourier transform $z \to q_i$ in the vorticity dimension using a standard NAG routine [40], and solving the resulting problem using a semi-implicit Crank-Nicolson algorithm [38]

$$\boldsymbol{\Sigma}_{ij}^{n+1} - \boldsymbol{\Sigma}_{ij}^{n+2/3} = \frac{1}{2}l^2\Delta t(\partial_y^2 \boldsymbol{\Sigma}_{ij}^{n+2/3} - q_i^2 \boldsymbol{\Sigma}_{ij}^{n+2/3}) + \frac{1}{2}l^2\Delta t(\partial_y^2 \boldsymbol{\Sigma}_{ij}^{n+1} - q_i^2 \boldsymbol{\Sigma}_{ij}^{n+1}), \tag{17}$$

in which the index i now labels the Fourier mode number. The derivatives ∂_y^2 are discretized as in Eq. (10) above. Note that Eq. (17) contains no mixing of the Cartesian components $\Sigma_{\alpha\beta}$ for any $\alpha\beta = xx, xy, yy, \ldots$, so can be solved for each one separately. Bringing all terms in the unknown $\boldsymbol{\Sigma}_{ij}^{n+1}$ across to the left hand side, and putting all terms in the known $\boldsymbol{\Sigma}_{ij}^{n+2/3}$ on the right-hand side, we obtain a sparse set of linear equations characterized by a tridiagonal matrix on the left hand side. These are then solved for the $\boldsymbol{\Sigma}_{ij}^{n+1}$ using standard NAG routines [40].

Having updated $\boldsymbol{\Sigma}^n \to \boldsymbol{\Sigma}^{n+1}$ using the viscoelastic constitutive equation, we now update the stream functions ϕ^n, $\psi^n \to \phi^{n+1}$, ψ^{n+1} using the x, y, and z components of the force balance equation (4). Again, we work in real flow-gradient space and reciprocal vorticity space. To eliminate the pressure from Eq. (4), we subtract ∂_y of the z component from ∂_z of the y component to get the following equations, written separately for $q_i = 0$ and $q_i \neq 0$:

$$\partial_y^3 \phi|_{0(j+1/2)}^{n+1} = -\frac{1}{\eta}\,\partial_y \Sigma_{xy}|_{0(j+1/2)}^{n+1} \quad \text{for} \quad q_i = 0, \tag{18}$$

$$\partial_y^3 \phi|_{i(j+1/2)}^{n+1} - q_i^2\,\partial_y \phi|_{i(j+1/2)}^{n+1} = -\frac{1}{\eta}\left(\partial_y \Sigma_{xy}|_{i(j+1/2)}^{n+1} + iq_i \Sigma_{xz}|_{i(j+1/2)}^{n+1}\right) \quad \text{for} \quad q_i \neq 0, \tag{19}$$

$$\partial_y^3 \psi|_{0(j+1/2)}^{n+1} = \frac{1}{\eta}\,\partial_y \Sigma_{yz}|_{0(j+1/2)}^{n+1} \quad \text{for} \quad q_i = 0, \tag{20}$$

$$\nabla^4 \psi|_{ij}^{n+1} = -\frac{1}{\eta}\left[iq_i \partial_y (\Sigma_{yy} - \Sigma_{zz})\big|_{ij}^{n+1} - (q_i^2 + \partial_y^2)\Sigma_{yz}\big|_{ij}^{n+1}\right] \quad \text{for} \quad q_i \neq 0, \tag{21}$$

with $\nabla^2 = (\partial_y^2 - q_i^2)$. The real and imaginary parts of these equations are treated separately. The third order equations (18)–(20) are discretized at staggered half grid points $y_{j+1/2}$ for $j = 1, \ldots, N_y - 1$, with derivatives calculated as follows:

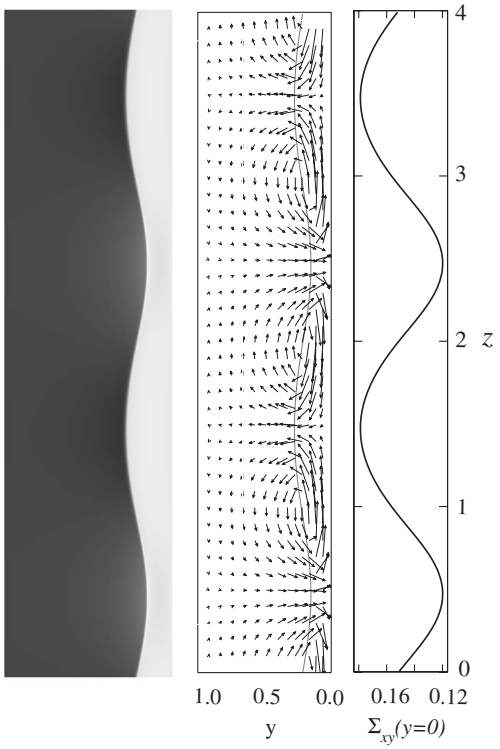

FIG. 3. Steady state at $a=0.3$, $\eta=0.05$, $\dot{\bar{\gamma}}=2.0$, $l=0.00375$, $L_z=4.0$. Left: greyscale of Σ_{xx} in the y-z plane. Middle: $(y-z)$ velocity vectors, showing roll states. Right: vorticity banding of viscoelastic shear stress.

$$\partial_y f|_{j+1/2} = \frac{1}{\Delta y}(f_{j+1} - f_j) \tag{22}$$

and

$$\partial_y^3 f|_{j+1/2} = \frac{1}{(\Delta y)^3}(f_{j+2} - 3f_{j+1} + 3f_j - f_{j-1}) \tag{23}$$

for any quantity f. (For clarity, the subscript i and the superscript n have been omitted from these expressions.) The fourth order equation is implemented at full grid points y_j, excluding those at the very edge of the domain (y_0 and y_N). In it, ∂_y^2 and ∂_y are discretized as in Eqs. (10) and (14), respectively, and ∂_y^4 according to

$$\partial_y^4 f|_j = \frac{1}{(\Delta y)^4}(f_{j+2} - 4f_{j+1} + 6f_j - 4f_{j-1} + f_{j-2}), \tag{24}$$

Each of Eqs. (18)–(21), for each mode index i, then takes the form of a sparse set of linear equations for ϕ_{ij}^{n+1} or ψ_{ij}^{n+1}. These equations are solved using standard NAG routines [40].

It remains finally to specify the spatial discretization of the boundary conditions. In turn, this will prescribe the values of the flow variables on the phantom grid points that lie just outside the flow domain.

In the vorticity direction z, the boundary conditions are periodic. For any quantity f on the grid $z_1, \ldots, z_{N_Z}$, in real space z_i, we thus have $f_{-1} = f_{N_z-1}$, $f_0 = f_{N_Z}$, $f_{N_z+1} = f_0$, $f_{N_z+2} = f_1$. In reciprocal space q_i, the periodic boundary conditions are always satisfied.

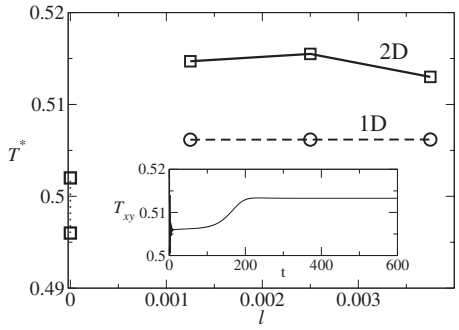

FIG. 4. Selected stress: 1D initial state and 2D steady state. $L_z=2.0$, $a=0.3$, $\eta=0.05$, $\bar{\dot{\gamma}}=2.0$. At $l=0$, the stress varies erratically about an average that depends on the grid. Inset: evolution to steady state at $l=0.00375$.

In the flow-gradient direction y, the boundary conditions for the fluid velocity at the plates $y=0,1$ are those of no slip and no permeation. In terms of the stream function ϕ, the no slip condition gives $\partial_y\phi=0$ at $y=0$ and $\partial_y\phi=\bar{\dot{\gamma}}$ at $y=1$. We also note that ϕ is only defined up to an arbitrary additive constant, and accordingly choose $\phi=0$ at $y=0$. The third order Eqs. (18) and (19) then have three boundary conditions, as required. After discretizing real flow-gradient space y_j in reciprocal vorticity space q_i, we then have

$$\phi_{i1}=0, \quad \phi_{i0}=\phi_{i2}, \quad \text{and} \quad \phi_{i(N_y+1)}=\phi_{i(N_y-1)}+\delta_{i0}\bar{\dot{\gamma}}\Delta y,$$

in which δ_{ij} is the usual Kronecker delta function.

In terms of the stream function ψ, the no-slip condition gives $\partial_y\psi=0$ at $y=0,1$, and the no-permeation condition gives $\partial_z\psi=0$ at $y=0,1$. We also note that ψ is only defined up to an arbitrary additive constant, and choose $\psi=0$ at $y=0$. In the $q_i=0$ Eq. (20), we then have

$$\psi_{i1}=0, \quad \psi_{i0}=\psi_{i2}, \quad \text{and} \quad \psi_{i(N_y+1)}=\psi_{i(N_y-1)}.$$

These also hold for the $q_i\neq 0$ equation (21), which obeys the additional condition

$$\psi_{iN_y}=0.$$

The zero-gradient boundary condition for the viscoelastic stress, after discretization on the flow-gradient grid $y_1,y_2,\ldots,y_{N_y}$, gives $f_{i0}=f_{i2}$ and $f_{i(N_y+1)}=f_{i(N_y-1)}$ for all components $f=\Sigma_{xx}$, Σ_{xy}, Σ_{yy}, … . These apply in both real z_i and reciprocal q_i vorticity spaces.

Extension to the case of a nonlinear grid in the y direction is straightforward in principle, but cumbersome in detail. Discretized derivatives are calculated via the usual Taylor expansions. For example, to first order accuracy, centred second derivatives with respect to y become

$$\partial_y^2 f_j=\frac{2}{y_{j+1}-y_{j-1}}\left[\frac{f_{j+1}-f_j}{y_{j+1}-y_j}-\frac{f_j-f_{j-1}}{y_j-y_{j-1}}\right]. \tag{25}$$

We checked our nonlinear mapping carefully by performing a few runs for identical parameter sets with both linear and highly nonlinear grids. All the numerical results in this paper are converged with respect to grid and timestep, to within the accuracy resolvable on the plots presented.

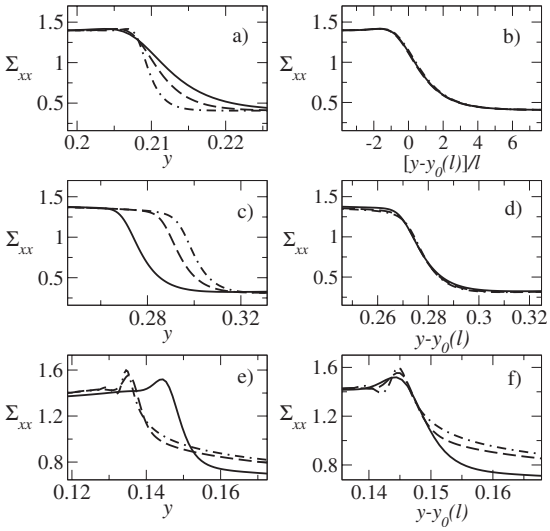

FIG. 5. Profile Σ_{xx} normal to the interface; $l=0.00375$ (solid lines), $l=0.00250$ (dashed lines), 0.00125 (dot-dashed lines). $a=0.3$, $\eta=0.05$, $\bar{\dot{\gamma}}=2.0$, $L_z=2.0$. (a),(b) 1D state with interfacial thickness $d\propto l$. (c),(d); (e),(f) 2D state at the z coordinate where the interface has maximal + and $-y$ displacements. The thickness d appears *independent* of l, but note the bump of thickness $O(l)$. The offset $y_0(l)$ is chosen to center the profile at the same location in each case.

VI. NONLINEAR STEADY STATE

In each simulation run, we input as an initial condition the 1D gradient-banded state discussed in Sec. III, superposed with Fourier perturbations of tiny random amplitudes. As expected, under conditions where the linear analysis of Sec. IV predicts the 1D initial state to be unstable with respect to perturbations with wave vectors $\mathbf{q}=q_z\hat{\mathbf{z}}$ in the vorticity direction, we find that these initial disturbances grow in time. Full agreement between (i) the early-time growth rate and functional form of the fastest growing mode and (ii) the most unstable eigenvalue and eigenfunction of the linear stability analysis provides a stringent check of our numerical method.

During the instability, the initially flat interface between the bands develops undulations that grow in time. At long times, once nonlinear effects become important, these saturate in a finite amplitude interfacial undulation to give a 2D steady state (Fig. 3). The wavelength of the steady undulations corresponds to that of the maximally unstable mode of the linear analysis. For the parameters of Fig. 3, this is roughly twice the gap width. Associated with these undulations are velocity rolls stacked in the vorticity direction (Fig. 3, middle), accompanied by undulations of the stress along the wall (Fig. 3, right). The results of Fig. 3 could be tested experimentally as follows. Optical measurements should reveal birefringent stripes stacked in the vorticity direction, each of height comparable to the gap width. Likewise, the velocity rolls could be measured using velocimetry. This is a challenging task, however, because the highest speed in Fig. 3(c) is only $O(0.01)$.

Our results capture recent experimental observations in which an initially 1D gradient banded state of a wormlike surfactant solution was found to destabilize with respect to interfacial undulations with wavevector in the vorticity direction [27]. Indeed, several features of our results can be directly compared with these experiments, as follows. In the ultimate steady state, the wavelength $O(L)$ and amplitude $O(L/10)$ of the undulations in our Fig. 3 are comparable to those in Fig. 2 of Ref. [27], measured in units of the gap width L. The wavelength of these undulations was furthermore reported to increase with increasing average applied shear rate $\bar{\dot{\gamma}}$ [27], consistent with the inset of our Fig. 2(b).

The kinetics of the instability can also be compared, via the temporal evolution of the stress signal. In the experiments [27], a shear startup protocol was followed. Accordingly, the stress signal showed an initial overshoot followed by a decay (at $\bar{\dot{\gamma}}=30\ \mathrm{s}^{-1}$) on a time scale $O(\tau)$ to a plateau value. This part of the dynamics corresponded to the initial formation of 1D gradient bands. It is absent from our simulations, because we take as our initial condition an already 1D gradient banded flow. Subsequently, the stress signal in Ref. [27] slowly increased by about 1% on a time scale $O(100\tau)$. This part of the dynamics was associated with the 1D gradient banded state destabilising to exhibit vorticity undulations. As shown in Fig. 4, it is captured very well by our simulations: we find a slow stress increase $O(1\%)$ on a time scale $O(100\tau)$, consistent with the experiments.

Some differences between our work and the experiments of Ref. [27] are noted as follows. In Ref. [27], the instability was studied using light scattering techniques, which couple to concentration fluctuations. In the present manuscript, we do not consider concentration coupling. In future work, it might be interesting to perform analogous simulations in the concentration coupled model of Ref. [41]. However, an important finding of the present work is that concentration coupling is not actually needed to trigger the basic undulatory instability. Indeed, we believe this to stem instead from normal stress effects, with concentration coupling a subdominant feature. Finally, we have not seen the exotic dynamics reported at the edges of the stress plateau in Ref. [27]. We cannot numerically access small enough l for the instability to persist here [recall Fig. 2(b)].

We return to comment on the validity of restricting our study to the y-z plane, which was done mainly for computational efficiency. As seen from our results, the ultimate amplitude of the interfacial undulation in this y-z plane is in fact comparable to that reported in the x-y plane in Ref. [34] (to within 10% at $a=0.3$, $\eta=0.05$, $\bar{\dot{\gamma}}=2.0$, $l=0.00375$, $L_{\{x,z\}}=2$). The present study therefore shows that vorticity structuring is indeed important, but also that a full 3D simulation should be performed in future work.

Finally, we discuss briefly the thickness d of the interface between the bands. In the 1D initial state, $d=O(l)$. In the limit $l\to 0$, this gives an unphysically sharp interface $d\to 0$. Associated with this is a pathological steady state that depends strongly on the flow history [42]. In 2D, in contrast, d appears virtually independent of l, as shown in Figs. 5(c)–5(f). This is an important finding that could potentially obviate the gradient term $l^2\nabla^2\Sigma$ in Eq. (3), which is needed to give a finite interfacial thickness in 1D [15]. Nonetheless, the interfacial profile does retain a small bump of thickness $O(l)$, Figs. 5(e) and 5(f), suggesting that the local case $l=0$ remains pathological even in 2D. Indeed, at $l=0$ the stress signal varies erratically about an average that varies between runs, Fig. 4, though purely numerical instability cannot be ruled out. This important issue will be pursued further in future work.

To summarize, we have identified a mechanism by which vorticity stress bands and velocity rolls can form in a complex fluid, triggered by the instability of gradient shear banded flow with respect to interfacial undulations. In any real startup experiment, we would expect the vorticity instability to commence during the final stages of the initial band formation: above we assumed a complete separation of timescales between the processes. In future work, we will study the true dynamics of shear startup experiment in curved Couette flow. We will also extend to 3D, to study the interplay of vorticity banding with the dynamics of Ref. [34]. Robustness of the mechanism in other models will also be studied.

ACKNOWLEDGMENTS

The author thanks Peter Olmsted, Paul Callaghan, Georgina Wilkins and Helen Wilson for discussions, and the UK's EPSRC for financial support, Grant No. GR/S29560/01.

[1] M. M. Britton and P. T. Callaghan, Phys. Rev. Lett. **78**, 4930 (1997).
[2] J. F. Berret, G. Porte, and J. P. Decruppe, Phys. Rev. E **55**, 1668 (1997).
[3] L. Becu, S. Manneville, and A. Colin, Phys. Rev. Lett. **93**, 018301 (2004).
[4] O. Diat, D. Roux, and F. Nallet, J. Phys. II **3**, 1427 (1993).
[5] G. M. H. Wilkins and P. D. Olmsted, 21, 133 (2006).
[6] J. B. Salmon, S. Manneville, and A. Colin, Phys. Rev. E **68**, 051503 (2003).
[7] C. Pujolle-Robic and L. Noirez, Nature (London) **409**, 167 (2001).
[8] M. P. Lettinga and J. K. G. Dhont, J. Phys.: Condens. Matter **16**, S3929 (2004).
[9] J. K. G. Dhont, M. P. Lettinga, Z. Dogic, T. A. J. Lenstra, H. Wang, S. Rathgeber, P. Carletto, L. Willner, H. Frielinghaus, and P. Lindner, Faraday Discuss. **123**, 157 (2003).
[10] J. F. Berret and Y. Serero, Phys. Rev. Lett. **87**, 048303 (2001).
[11] P. Coussot, J. S. Raynaud, F. Bertrand, P. Moucheront, J. P. Guilbaud, H. T. Huynh, S. Jarny, and D. Lesueur, Phys. Rev. Lett. **88**, 218301 (2002).
[12] L. Hilliou and D. Vlassopoulos, Ind. Eng. Chem. Res. **41**,

6246 (2002).
[13] L. B. Chen, C. F. Zukoski, B. J. Ackerson, H. J. M. Hanley, G. C. Straty, J. Barker, and C. J. Glinka, Phys. Rev. Lett. **69**, 688 (1992).
[14] J. Yerushalmi, S. Katz, and R. Shinnar, Chem. Eng. Sci. **25**, 1891 (1970).
[15] C. Y. David Lu, P. D. Olmsted, and R. C. Ball, Phys. Rev. Lett. **84**, 642 (2000).
[16] D. Bonn, J. Meunier, O. Greffier, A. Al-Kahwaji, and H. Kellay, Phys. Rev. E **58**, 2115 (1998).
[17] P. Fischer, E. K. Wheeler, and G. G. Fuller, Rheol. Acta **41**, 35 (2002).
[18] P. Fischer, Rheol. Acta **39**, 234 (2000).
[19] J. L. Goveas and P. D. Olmsted, Eur. Phys. J. E **6**, 79 (2001).
[20] P. D. Olmsted and C. Y. David Lu, Phys. Rev. E **60**, 4397 (1999).
[21] P. G. Drazin and W. H. Reid, *Hydrodynamic Stability* (Cambridge University Press, Cambridge, 2004).
[22] R. G. Larson, E. S. G. Shaqfeh, and S. J. Muller, J. Fluid Mech. **218**, 573 (1990).
[23] R. G. Larson, Rheol. Acta **31**, 213 (1992).
[24] K. G. Kang, M. P. Lettinga, Z. Dogic, and J. K. G. Dhont, Phys. Rev. E **74**, 026307 (2006).
[25] S. M. Fielding, Phys. Rev. Lett. **95**, 134501 (2005).
[26] H. J. Wilson and S. M. Fielding, J. Non-Newtonian Fluid Mech. **138**, 181 (2006).
[27] S. Lerouge, M. Argentina, and J. P. Decruppe, Phys. Rev. Lett. **96**, 088301 (2006).
[28] J. P. Decruppe, O. Greffier, S. Manneville, and S. Lerouge, Phys. Rev. E **73**, 061509 (2006).
[29] M. M. Britton and P. T. Callaghan, Phys. Rev. Lett. **78**, 4930 (1997).
[30] M. E. Cates, J. Phys. Chem. **94**, 371 (1990).
[31] M. W. Johnson and D. Segalman, J. Non-Newtonian Fluid Mech. **2**, 255 (1977).
[32] W. Yerushal, S. Katz, and R. Shinnar, Chem. Eng. Sci. **25**, 1891 (1970).
[33] Y. Y. Renardy, Theor. Comput. Fluid Dyn. **7**, 463 (1995).
[34] S. M. Fielding and P. D. Olmsted, Phys. Rev. Lett. **96**, 104502 (2006).
[35] E. J. Hinch, O. J. Harris, and J. M. Rallison, J. Non-Newtonian Fluid Mech. **43**, 311 (1992).
[36] T. C. B. McLeish, J. Polym. Sci., Part B: Polym. Phys. **25**, 2253 (1987).
[37] M. D. Chilcott and J. M. Rallison, J. Non-Newtonian Fluid Mech. **29**, 381 (1988).
[38] W. H. Press, S. A. Teukolsky, W. T. Vetterling, and B. P. Flannery, *Numerical Recipes in C*, 2nd ed. (Cambridge University Press, Cambridge, 1992).
[39] C. Pozrikidis, *Introduction to Theoretical and Computation Fluid Dynamics* (Oxford University Press, New York, 1997).
[40] Numerical Algorithms Group Ltd., Wilkinson House, Jordan Hill Road, Oxford, OX2 8DR, UK.
[41] S. M. Fielding and P. D. Olmsted, Eur. Phys. J. E **11**, 65 (2003).
[42] P. D. Olmsted, O. Radulescu, and C. Y. D. Lu, J. Rheol. **44**, 257 (2000).